14th International Conference on Structural Safety and Reliability - ICOSSAR'25
1-6 June, 2025 - Los Angeles California, USA
R. Ghanem, E. Johnson, S. Masri and A. Olivier (Eds)

RELIABILITY-BASED MULTILATTICE TOPOLOGY OPTIMIZATION FOR STRUCTURAL DESIGN

Junho Chun[1]

[1] School of Architecture, Syracuse University
146 College Pl, Syracuse, NY 13210, USA
jchun04@syr.edu

Key words: Lattice structure, Topology optimization, reliablity-based topology optimization, multi-material, surrogate model

Abstract. This paper presents a reliability-based multilattice topology optimization framework for structural design under uncertainty in material properties. Many natural and engineered materials—such as bone, wood, and polymers—possess hierarchical microstructures and spatially varying mechanical properties, enabling multifunctionality and adaptability. Inspired by these systems, architected lattice materials (also known as metamaterials) are engineered to achieve tunable mechanical performance through controlled porosity and microstructural orientation. These attributes enable the design of heterogeneous, high-performance systems that surpass the capabilities of their individual constituents. Topology optimization (TO) serves as a powerful tool for designing structures with spatially tailored material distributions and hierarchical configurations. However, computing the effective properties of lattice unit cells via homogenization at every optimization step is computationally intensive. To address this challenge, we propose a density-based TO framework that incorporates multiple lattice structures while accounting for material uncertainty. A Kriging-based surrogate modeling approach is employed to efficiently estimate the effective behavior of lattice structures across a range of relative densities, significantly reducing computational effort. Numerical examples involving multiscale lattice configurations demonstrate the feasibility and effectiveness of the proposed framework in generating lightweight, structurally robust designs under probabilistic constraints. The approach provides a scalable solution for engineering applications demanding high performance, adaptability, and resilience under uncertainty.

1 INTRODUCTION

Topology optimization (TO) is a computational method used to determine the optimal material distribution within a given design domain, typically by minimizing structural compliance subject to constraints such as material volume, stress, or stability [1]. TO has been widely applied across engineering fields, including mechanical [2], aerospace [3], biomedical [4], and civil engineering [5, 6]. Recent developments have extended TO to multi-material and lattice-based designs, enabling optimized spatial allocation of materials for multifunctional performance such as stiffness, energy absorption, or negative Poisson's ratio [7, 8]. Lattice structures, in particular, offer high stiffness-to-weight ratios and are well-suited for additive manufacturing. Their integration into TO has been explored through homogenization-based modeling [9] and more recently, through data-driven and surrogate

modeling techniques to reduce computational cost [10]. This study builds upon recent advances by integrating Kriging-based surrogate models into a density-based topology optimization framework to efficiently approximate the effective mechanical behavior of anisotropic lattice structures across varying densities. To address uncertainties in material properties and loading conditions, a reliability-based topology optimization approach is incorporated. The proposed Reliability-Based Multi-Lattice Topology Optimization (RBMTO) method enables the reliable design of structures through the spatial allocation of multiple lattice types, tailored to meet diverse performance and reliability requirements.

2 RELIABILITY-BASED MULTI-MATERIAL TOPOLOGY OPTIMIZATION

The problem of minimizing compliance in topology optimization seeks to determine the stiffest material layout within a prescribed design domain, subject to applied loads and boundary conditions. It is formulated as:

$$\begin{aligned} \inf_{\boldsymbol{\rho}} \quad & J(\boldsymbol{\rho}) = \int_{\Gamma_t} \mathbf{t} \cdot \mathbf{u}\, ds = \int_{\Omega} \mathbf{C}(\boldsymbol{\rho})\, \boldsymbol{\varepsilon}(\mathbf{u}) : \boldsymbol{\varepsilon}(\mathbf{u})\, d\mathbf{x} \\ \text{subject to} \quad & g(\boldsymbol{\rho}) = \frac{1}{|\Omega|} \int_{\Omega} m_v(\boldsymbol{\rho})\, d\mathbf{x} - \overline{V}_f \leq 0 \end{aligned} \tag{1}$$

In this formulation, $\mathbf{C}(\boldsymbol{\rho})$ is the material elasticity tensor, which depends on the density function $\boldsymbol{\rho}(\mathbf{x}) \in [0,1]$. The domain Ω denotes the design region, and its boundary $\partial\Omega$ is partitioned into displacement boundaries Γ_D and traction boundaries Γ_t and Γ_{t0}, as illustrated in Figure 1. The strain tensor is defined as $\boldsymbol{\varepsilon}(\mathbf{u}) = \frac{1}{2}(\nabla\mathbf{u} + \nabla\mathbf{u}^T)$, and $\mathcal{V}$ denotes the space of admissible displacements. The term $\overline{V}_f$ represents the prescribed maximum volume fraction, $|\Omega|$ is the volume of the design domain, and $m_v(\boldsymbol{\rho})$ is the interpolation function used in the volume constraint.

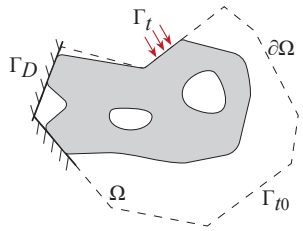

Figure 1: Illustration of the prescribed boundary conditions on the design domain Ω. The boundary $\partial\Omega$ consists of the displacement boundary Γ_D, the homogeneous traction boundary Γ_{t0}, and the non-homogeneous traction boundary Γ_t. The converged topology is illustrated in grey.

2.1 Multi-Lattice Topology Optimization

The volume-constrained compliance minimization problem for multi-lattice topology optimization, following [8], is formulated as:

$$\begin{aligned} \min_{\mathbf{z}_1,\cdots,\mathbf{z}_m} \quad & J = \mathbf{f}^T \mathbf{u}(\mathbf{z}_1, \cdots, \mathbf{z}_m) \\ \text{subject to} \quad & g_k = \sum_{i \in \eta_k} \sum_{e \in \chi_k} \hat{\rho}_i^e V^e - \overline{V}_k \leq 0, \quad k = 1, \cdots, N_c \\ & 0 \leq \rho_i^e \leq 1, \quad i = 1, \cdots, m, \quad e = 1, \cdots, N_e \\ \text{with} \quad & \mathbf{K}(\mathbf{z}_1, \cdots, \mathbf{z}_m)\, \mathbf{u}(\mathbf{z}_1, \cdots, \mathbf{z}_m) = \mathbf{f} \end{aligned} \tag{2}$$

Here, g_k denotes the volume constraint associated with the k^{th} region. The variables $\mathbf{z}_1, \cdots, \mathbf{z}_m$ represent the density fields for m different lattice structures in the discretized design domain. The set η_k contains the indices of lattice materials subject to constraint k, while χ_k defines the set of element indices relevant to that constraint. The term $\hat{\rho}_i^e$ is the filtered density of lattice structure i in element e, and V^e is the area (in 2D) or volume (in 3D) of element e. The parameter _

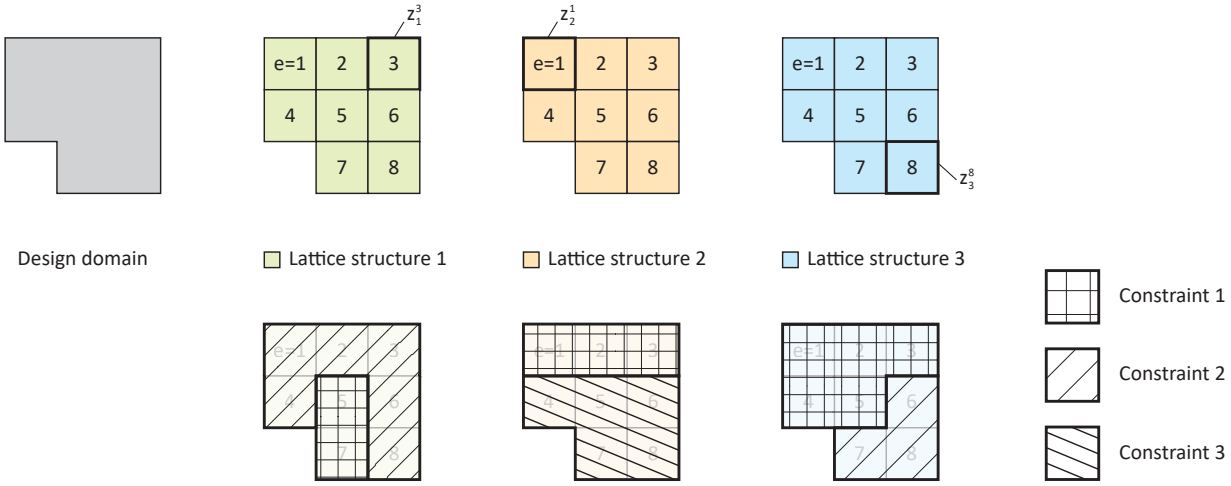

Figure 2: Illustration of the design domain, discretized elements (lattice structure unit cell), three lattice structures, and constraints in multi-lattice TO. Design space is discretized with eight elements and there are three candidate lattice structures and three constraints.

In multi-lattice TO, the set of elasticity tensors of m lattice structures at each elemental point is

$$\mathcal{S}(\mathbf{x}) = \{\mathbf{C}_1(\mathbf{x}), \cdots, \mathbf{C}_m(\mathbf{x})\} \tag{3}$$

The elastic tensor $\mathbf{C}(\mathbf{x})$ is defined by choosing a finite set of m lattice structures such as

$$\mathbf{C}(\mathbf{x}) = \mathcal{A}\left(\mathcal{S}(\mathbf{x})\right) \tag{4}$$

The filtered density of lattice unit cell i is obtained

$$\hat{\boldsymbol{\rho}}_i(\mathbf{x}) = \mathbf{P}\mathbf{z}_i(\mathbf{x}), \quad i = 1, \cdots, m \tag{5}$$

2.2 Reliability-Based Multi-Lattice Topology Optimization

Reliability-Based Topology Optimization (RBTO) for linear elastic systems with probabilistic constraints is formulated as follows (where $\bar{\boldsymbol{\rho}} \equiv [\bar{\boldsymbol{\rho}}_1, \cdots, \bar{\boldsymbol{\rho}}_m]$):

$$\begin{aligned} \min_{\mathbf{z}_1,\cdots,\mathbf{z}_m} \quad & f(\bar{\boldsymbol{\rho}}, \boldsymbol{\mu}_\psi) \\ \text{subject to} \quad & P\left[g_i(\bar{\boldsymbol{\rho}}, \psi) \leq 0\right] \leq P^t, \quad i = 1, \ldots, N_c \\ \text{with} \quad & \mathbf{K}(\bar{\boldsymbol{\rho}}, \psi)\, \mathbf{u}(\bar{\boldsymbol{\rho}}, \psi) = \mathbf{f}(\psi) \end{aligned} \tag{6}$$

where g_i denotes the i^{th} limit-state function, whose violation (i.e., $g_i \leq 0$) corresponds to failure. The probability operator $P[\cdot]$ quantifies the likelihood of constraint violation, ψ is the vector of random variables, $\boldsymbol{\mu}_\psi$ is the vector of their means, and P^t is the target failure probability. The probabilistic

constraint in Eq. (6) can be rewritten using the cumulative distribution function (CDF) of the limit-state function:

$$P\left[g_i \leq 0\right] = F_{g_i}(0) \leq \Phi(-\beta_i^t) \tag{7}$$

where $F_{g_i}(\cdot)$ is the CDF of the i^{th} limit-state function, $\Phi(\cdot)$ is the standard normal CDF, and β_i^t is the target reliability index. The failure probability can be evaluated using the First-Order or Second-Order Reliability Method (FORM/SORM) [12]. To reduce the computational cost of nested optimization in Eq. (6), a single-loop approximation approach is adopted. The resulting single-loop RBMTO formulation is:

$$\begin{aligned} \min_{\mathbf{z}_1,\cdots,\mathbf{z}_m} \quad & f(\bar{\boldsymbol{\rho}}, \boldsymbol{\mu}_\psi) \\ \text{subject to} \quad & g_{p_i} \approx g_i(\bar{\boldsymbol{\rho}}, \psi(\tilde{\mathbf{U}}_i^t)) \geq 0, \quad i = 1, \ldots, N_c \\ \text{with} \quad & \mathbf{K}(\bar{\boldsymbol{\rho}}, \psi(\tilde{\mathbf{U}}_i^t))\, \mathbf{u}(\bar{\boldsymbol{\rho}}, \psi(\tilde{\mathbf{U}}_i^t)) = \mathbf{f}(\psi(\tilde{\mathbf{U}}_i^t)) \end{aligned} \tag{8}$$

Here, $\tilde{\mathbf{U}}_i^t$ is the approximated most probable point (MPP) for the i^{th} limit-state function, given by:

$$\tilde{\mathbf{U}}_i^t \approx \beta_i^t \widehat{\boldsymbol{\alpha}}_i^t = \beta_i^t \left[-\frac{\nabla_\psi g_i(\bar{\boldsymbol{\rho}}, \psi(\mathbf{U}))\, \mathbf{J}_{\psi,\mathbf{U}}}{\|\nabla_\psi g_i(\bar{\boldsymbol{\rho}}, \psi(\mathbf{U}))\, \mathbf{J}_{\psi,\mathbf{U}}\|} \right]_{\mathbf{U}=\tilde{\mathbf{U}}_i} \tag{9}$$

In this expression, $\mathbf{U}$ denotes the vector of standard normal variables, and $\mathbf{J}_{\psi,\mathbf{U}} = \mathbf{J}_{\mathbf{U},\psi}^{-1}$ is the Jacobian of the transformation from physical variables ψ to standard normal variables $\mathbf{U}$. The evaluation of the stiffness matrix $\mathbf{K}$ in the RBMTO formulation is discussed in the following section.

3 Homogenization

Homogenization [11] is a method used to compute the effective (macroscopic) properties of materials with heterogeneous or complex microstructures by averaging their local behavior. This process enables the derivation of equivalent material properties such as stiffness and thermal conductivity that can be used at the structural scale in engineering analysis and design. The effective elasticity tensor $\mathbb{C}^H$ of a periodic composite material can be computed by solving the homogenization problem:

$$\mathbb{C}^H = \frac{1}{|\Omega_u|} \int_{\Omega_u} \mathbb{C} \left(\mathbb{I} + \sum_{i,j} \nabla \boldsymbol{\chi}^{ij} \otimes \boldsymbol{\epsilon}_{ij} \right) dz \tag{10}$$

where $|\Omega_u|$ denotes the volume of the unit cell domain Ω_u, $\mathbb{I}$ is the fourth-order identity tensor, $\mathbb{C}$ is the local material elasticity tensor, and $\boldsymbol{\epsilon}_{ij}$ is a unit test strain field with the (i,j)-th component equal to one and all others zero. The function $\boldsymbol{\chi}^{ij}$ represents the periodic characteristic displacement field associated with $\boldsymbol{\epsilon}_{ij}$. The indices i, j range from 1 to 3 in 3D space. For a general anisotropic material, the fourth-order elasticity tensor has 21 independent components due to the following symmetry conditions:

$$C_{ijkl}^H = C_{klij}^H = C_{jikl}^H = C_{ijlk}^H \tag{11}$$

The remaining 60 components are derived from these symmetries. For isotropic or cubic-symmetric materials, the effective elasticity tensor can be expressed in Voigt notation as a 6×6 matrix:

$$\mathbb{C}^H = \begin{bmatrix} C_{11}^H & C_{12}^H & C_{13}^H & 0 & 0 & 0 \\ C_{21}^H & C_{22}^H & C_{23}^H & 0 & 0 & 0 \\ C_{31}^H & C_{32}^H & C_{33}^H & 0 & 0 & 0 \\ 0 & 0 & 0 & C_{44}^H & 0 & 0 \\ 0 & 0 & 0 & 0 & C_{55}^H & 0 \\ 0 & 0 & 0 & 0 & 0 & C_{66}^H \end{bmatrix} \tag{12}$$

The characteristic displacement fields $\boldsymbol{\chi}^{ij}$ are obtained by solving the unit cell (microstructure) problem with periodic boundary conditions, which require that opposite faces of the unit cell undergo compatible deformations under applied test strains. This condition ensures the continuity of displacements and traction equilibrium across the boundaries (see Figure 3).

$$\nabla \cdot \mathbb{C} \left[\nabla \boldsymbol{\chi}^{ij} + \boldsymbol{\epsilon}_{ij} \right] = \mathbf{0}, \quad \text{in } \Omega_u \tag{13}$$

In practice, homogenization is typically carried out numerically by discretizing the unit cell domain and solving the cell problems using the finite element method.

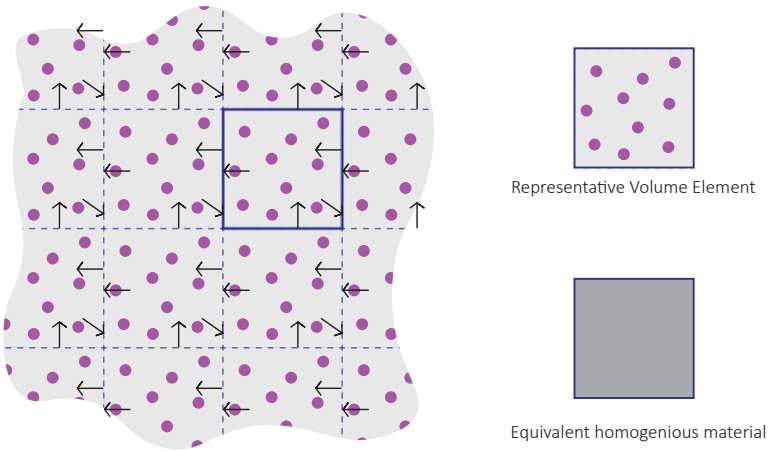

Figure 3: Illustration of a 2D periodic microstructure composed of two materials (gray and magenta). The solid blue line encloses the unit cell, and arrows indicate deformation under periodic boundary conditions.

3.1 Finite Element Model of a Lattice Structure

Numerical homogenization begins with the development of a finite element model of the lattice structure. First, a geometric model of the unit cell is created and then discretized using 3D solid elements. The unit cell is uniformly meshed, with each finite element having equal volume and size. Figure 4 shows the finite element meshes of representative lattice structures. Although mesh refinement studies are generally necessary to verify convergence in the components of the homogenized elasticity tensor $\mathbb{C}^H$, in this study, each unit cell is discretized using 70^3 solid elements (i.e., 70 elements along each spatial axis).

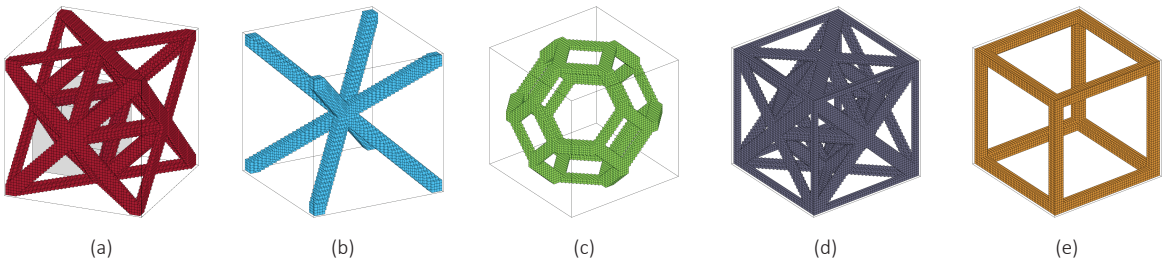

Figure 4: Finite element models of representative lattice structures: (a) octet structure, (b) asterisk structure, (c) tetrakaidecahedron structure, (d) enclosed octet structure, and (e) cubic structure.

3.2 Stiffness Matrix and Force Vector

In the finite element formulation of elasticity problems, the element stiffness matrix is computed as:

$$\hat{\mathbf{K}}_e = \int_{\Omega_e} \mathbf{C}_e \, \nabla \mathbf{N}_e : \nabla \mathbf{N}_e \, d\mathbf{x} \tag{14}$$

where $\mathbf{N}_e$ is the shape function matrix and $\mathbf{C}_e$ is the element-level constitutive matrix. For a cubic isotropic material, the constitutive matrix can be expressed using Lamé's parameters as:

$$\mathbf{C}_e = \begin{bmatrix} \lambda_e + 2\mu_e & \lambda_e & \lambda_e & 0 & 0 & 0 \\ \lambda_e & \lambda_e + 2\mu_e & \lambda_e & 0 & 0 & 0 \\ \lambda_e & \lambda_e & \lambda_e + 2\mu_e & 0 & 0 & 0 \\ 0 & 0 & 0 & \mu_e & 0 & 0 \\ 0 & 0 & 0 & 0 & \mu_e & 0 \\ 0 & 0 & 0 & 0 & 0 & \mu_e \end{bmatrix} \tag{15}$$

The Lamé parameters λ_e and μ_e are computed from Young's modulus E and Poisson's ratio ν as:

$$\lambda_e = \frac{\nu E}{(1+\nu)(1-2\nu)}, \quad \mu_e = \frac{E}{2(1+\nu)} \tag{16}$$

The global stiffness matrix for the unit cell is assembled by summing the element contributions:

$$\hat{\mathbf{K}} = \sum_{e=1}^{N_{ue}} \hat{\mathbf{K}}_e = \sum_{e=1}^{N_{ue}} \left(\lambda_e \hat{\mathbf{K}}_\lambda + \mu_e \hat{\mathbf{K}}_\mu \right) \tag{17}$$

where N_{ue} is the number of elements within the unit cell, and $\hat{\mathbf{K}}_\lambda$ and $\hat{\mathbf{K}}_\mu$ are stiffness matrices corresponding to unit Lamé parameters. The global force vector corresponding to a macroscopic strain field is given by:

$$\hat{\mathbf{f}}_j = \sum_k \int_{\Omega_k} \nabla \mathbf{N}_k \, \mathbf{C}_k \, \boldsymbol{\epsilon}_j \, d\Omega_k \tag{18}$$

where $\boldsymbol{\epsilon}_j$ is a unit strain vector defined as:

$$\boldsymbol{\epsilon}_1 = (1,0,0,0,0,0)^T, \quad \boldsymbol{\epsilon}_2 = (0,1,0,0,0,0)^T, \quad \ldots, \quad \boldsymbol{\epsilon}_6 = (0,0,0,0,0,1)^T \tag{19}$$

Using Lamé's parameters, the global force vector can be similarly expressed as:

$$\hat{\mathbf{f}}_j = \sum_k \left(\lambda_k \hat{\mathbf{f}}_{j,\lambda} + \mu_k \hat{\mathbf{f}}_{j,\mu} \right) \tag{20}$$

The characteristic displacements $\boldsymbol{\chi}_j$ for the cell problem in Eq. (13) are obtained by solving the following finite element equation:

$$\hat{\mathbf{K}}\,\boldsymbol{\chi}_j = \hat{\mathbf{f}}_j \tag{21}$$

Solving Eq. (21) for all six unit strain vectors defined in Eq. (19) yields the full set of characteristic displacement fields. These are then used to compute the homogenized constitutive matrix $\mathbb{C}^H$ as described in Eq. (12).

4 Surrogate Modeling

During the topology optimization process, the design variable, material density, is updated across all finite elements. Each finite element corresponds to a unit cell of a lattice structure. As the density is iteratively adjusted using a gradient-based optimization algorithm, the thickness of the lattice members is updated accordingly, necessitating the recalculation of the constitutive matrix for each unit cell. However, since the design variable varies continuously between 0 and 1, updating the constitutive matrix at every iteration would theoretically be required. This procedure is computationally prohibitive, especially considering that each unit cell in this study is discretized into $70 \times 70 \times 70$ solid elements, totaling 343,000 elements per cell. Moreover, the entire design domain is finely discretized to ensure high-resolution results. As a result, solving the unit cell problems defined in Eq. (21) for such a large number of cells with varying densities becomes impractical. To overcome this challenge, surrogate modeling techniques are introduced, specifically, the Kriging method. Kriging [13] is a stochastic interpolation approach that assumes the model output, $\mathcal{Y} = \Gamma(\mathbf{x})$, is a realization of a Gaussian process indexed by the input vector $\mathbf{x} \in D_{\mathbf{x}} \subset \mathbb{R}^M$. The Kriging approximation is given by:

$$\mathcal{Y} \approx \Gamma^{\text{Krig}}(\mathbf{x}) = \mathbf{m}^T\mathbf{f}(\mathbf{x}) + \sigma^2\kappa(\mathbf{x}, \mathbf{x}'; \boldsymbol{\Theta}) \tag{22}$$

where $\mathbf{m}^T\mathbf{f}(\mathbf{x})$ represents the mean response constructed from a set of basis functions f_j ($j = 1, \ldots, q$) and their associated coefficients m_j. The scalar σ^2 denotes the process variance, and $\kappa(\mathbf{x}, \mathbf{x}'; \boldsymbol{\Theta})$ is the covariance (or kernel) function, which defines a stationary Gaussian process with zero mean and unit variance. The kernel is governed by hyperparameters $\boldsymbol{\Theta}$ that control correlation length scales and smoothness. In standard TO, when the element density $\rho = 1$, the unit cell is fully filled with the isotropic constituent material, with no voids. However, in this study, a modified density-volume relationship is adopted: the lattice structure occupies only 50% of the unit cell volume when the element density is 1. This reduction in relative density is achieved by adjusting the thickness of the lattice members accordingly. To construct the Kriging surrogate, constitutive matrices for lattice unit cells with varying relative densities (ranging from 0 to 0.5) are precomputed as part of an initial design of experiments. An active learning strategy is then employed to iteratively refine the Kriging model, enabling efficient approximation of the constitutive behavior throughout the topology optimization process.

4.1 Constitutive Matrices and Kriging Models

Five distinct lattice unit cells, each with dimensions of 1 in $\times$ 1 in $\times$ 1 in, as illustrated in Figure 4, are analyzed in this study. The base material properties are defined by a Young's modulus of 10,000 ksi and a Poisson's ratio of 0.3. For each unit cell, the constitutive stiffness matrix and the homogenized (effective) elastic modulus are computed as functions of relative density by adjusting the cross-sectional thicknesses of the lattice members. Kriging-based surrogate models are developed to

approximate these constitutive relationships and are used for both prediction and validation. Figures 5 and 6 show the computed constitutive matrices and effective moduli obtained through numerical homogenization and the corresponding Kriging predictions. The comparisons demonstrate a strong agreement between the surrogate models and the high-fidelity homogenization results, validating the accuracy and efficiency of the surrogate approach.

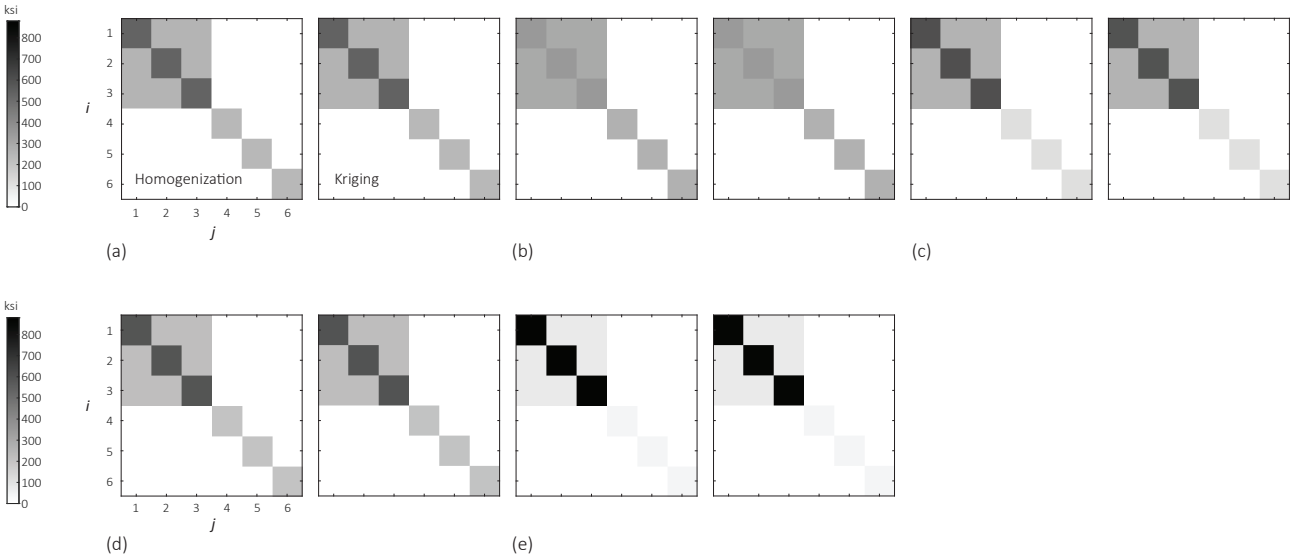

Figure 5: Constitutive matrices of lattice structures. a) octet structure, (b) asterisk structure, (c) tetrakaidecahedron, structure, (d) enclosed octet structure, and (e) cubic structure

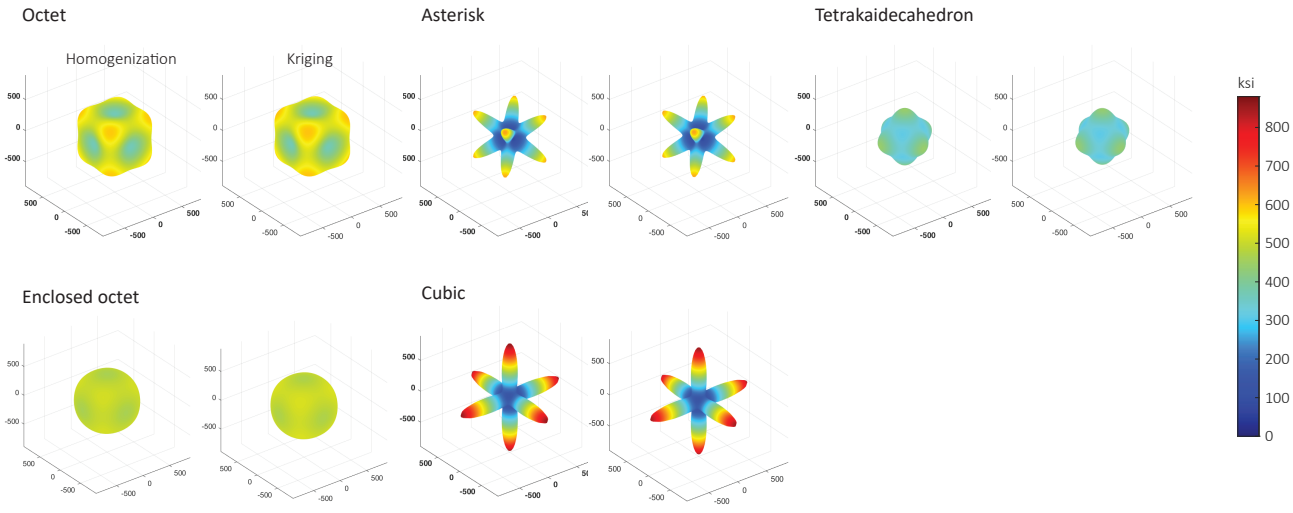

Figure 6: Effective modulus of elasticity of lattice structures with with about 19.1% relative density.

5 NUMERICAL APPLICATIONS

In two numerical applications, a Messerschmitt-Bölkow-Blohm (MBB) beam subjected to concentrated point loads illustrated in Figure 7 is considered. Five lattice structure configurations, each with

Table 1: Description of random variables of applied forces and Young's modulus for thhe MBB beam optimization

Random variable	Marginal distribution	Mean	c.o.v	Correlation
P_1	Log-normal	2 kips	0.1	$\rho_{P_1,P_2} = 0.25$
P_2	Log-normal	1 kip	0.1	
E	Normal	10,000 ksi	0.1	-

identical material properties, Young's modulus $E = 10,000$ and Poisson's ratio $\nu = 0.3$ are considered. Effective modulus of elasticity (E_{11}) of each lattice structure over relative densities is illustrated in Figure 7. In the proposed RBMTO framework, an element density of $\rho = 1.0$ corresponds to a

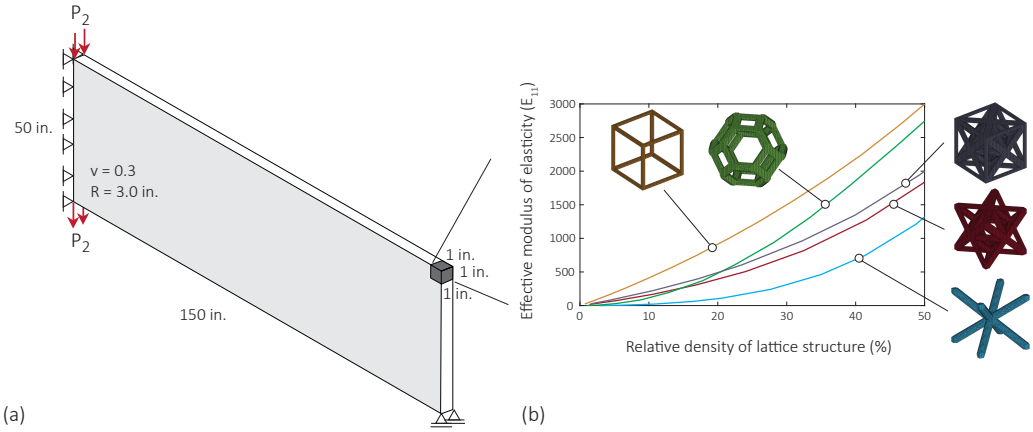

Figure 7: (a) Design domain with applied loading and boundary conditions. (b) Effective modulus of elasticity of the lattice structures as a function of relative density.

relative density of 50% for the lattice structure, while $\rho \simeq 0.0$ represents a void (zero relative density). The magnitudes of the applied forces (P_1, P_2) and the Young's modulus are modeled as independent random variables, each following a normal distribution. The statistical parameters, mean values and coefficients of variation for these random variables are summarized in Table 1.

5.1 Minimization of failure probability with volume constraints

The objective function is defined as the minimization of the failure probability associated with a compliance-based limit-state function, expressed as $P\,(\text{limit-state function: } J_{\max}(= 1.0) - J \leq 0)$. A global volume constraint of 0.5 is imposed, and the volume allocated to each lattice structure is therefore $0.5/5 = 0.1$. The failure probability is estimated using the FORM. The RBMTO results presented in Figure 8 indicate that the failure probability decreases when lattice structures (or their combinations) with higher effective elastic moduli are utilized. In contrast, incorporating lattice structures with lower effective moduli into topology optimization leads to an increase in the probability of failure. Next, the design domain of the MBB beam is partitioned into four distinct zones, with local volume constraints applied individually to each zone. A series of design scenarios is explored by assigning different combinations of lattice structures to the zones and adjusting the local volume limits accordingly. The zoning layout and the specific design cases considered are shown in Figure 9. Figure 10 presents the topology optimization results for three representative design cases. The observed topologies and the corresponding failure probabilities are influenced by the mechanical characteristics of the assigned lattice structures, as well as their local volume constraints. Specifically,

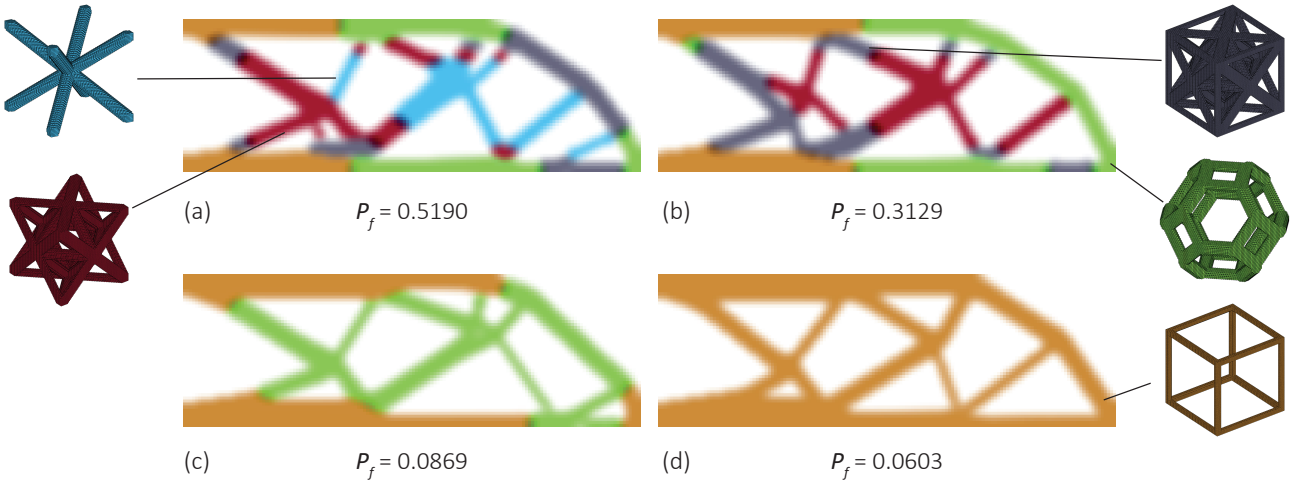

Figure 8: Results of the RBMTO procedure using different combinations and quantities of lattice structures. (a) Five lattice structures, each with a volume constraint of 0.1; (b) four lattice structures with a volume constraint of 0.125 each; (c) two lattice structures with a volume constraint of 0.25 each; and (d) one lattice structure occupying the full volume constraint.

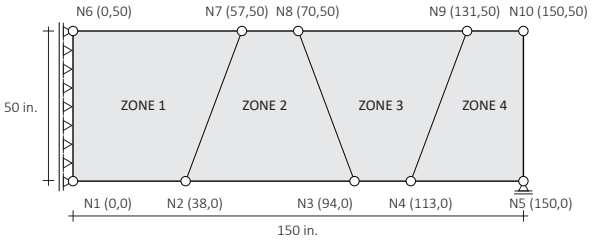

	CASE A		CASE B		CASE C	
	Lattice structure	Volume constraint	Lattice structure	Volume constraint	Lattice structure	Volume constraint
Zone 1	Cubic	0.45	Cubic	0.60	Octet	0.45
Zone 2	Tetra	0.45	Tetra	0.50	Tetra	0.45
Zone 3	Enclosed octet	0.45	Enclosed octet	0.40	Enclosed octet	0.45
Zone 4	Octet	0.45	Octet	0.30	Cubic	0.45

Figure 9: Zoning configuration of the MBB beam and corresponding design cases

zones assigned with stiffer lattice structures tend to reduce the probability of failure and contribute to a more efficient load design. In contrast, incorporating more compliant (lower modulus) lattice configurations or enforcing stricter volume constraints in critical load-bearing regions generally leads to increased failure risk and less optimal material distribution. These results highlight the importance of strategically allocating both material type and volume within the design domain to achieve reliability-aware optimization.

5.2 Minimization of Material Volume with Probabilistic Constraints

The same MBB beam configuration is employed in this application. The objective of the RBMTO framework is to minimize the total material volume while satisfying a probabilistic constraint corresponding to a specified target failure probability. The formulation uses the same set of random variables, material properties, and optimization parameters described earlier. All five lattice structures are considered, and the total material volume serving as the RBMTO objective is computed as the sum of the volumes corresponding to the lattice structures assigned to each finite element. Figure 11 presents the optimized topologies obtained for various target failure probability levels. A consistent trend is observed: stiffer lattice structures are preferentially placed near boundary conditions and in regions experiencing significant deformation. This targeted material distribution reduces structural compliance and helps lower the probability of failure. As the target failure probability be-

Figure 10: Topology optimization results. (a) Case A, (b) Case B, and (c) Case C

comes more relaxed, the optimization tends to utilize lattice structures with lower effective elastic moduli more frequently to reduce material usage. Although stiffer materials are generally more effective in enhancing reliability, the algorithm identifies a locally optimal configuration that balances reliability constraints and material efficiency. The reliability of the final optimized topologies is further validated through Monte Carlo simulation, confirming that the achieved failure probabilities are consistent with the target values.

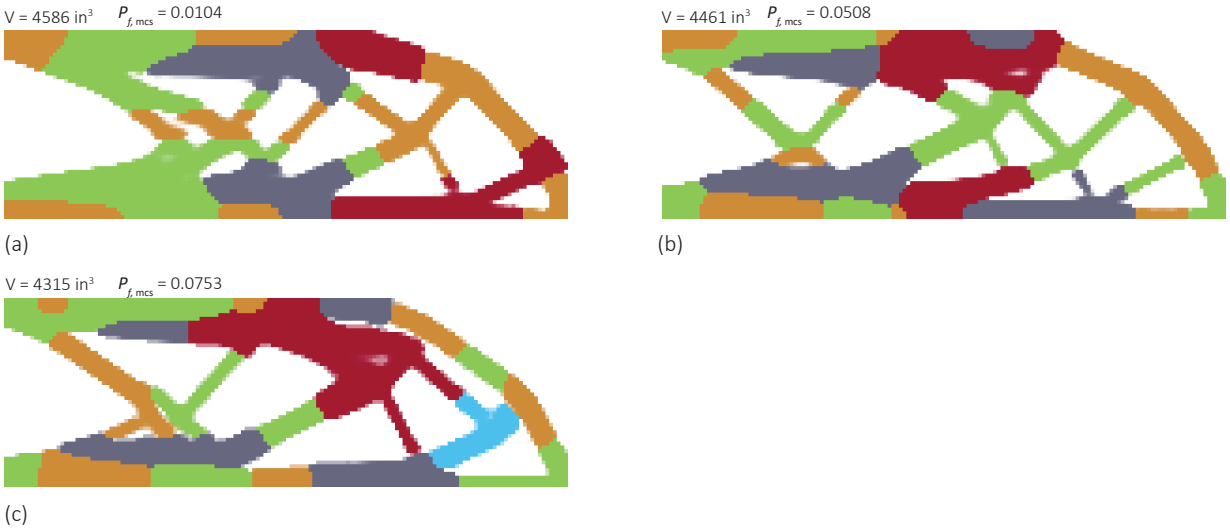

Figure 11: Optimal topologies under different target failure probabilities: (a) $P_f = 0.01$, (b) $P_f = 0.05$, and (c) $P_f = 0.075$

6 Conclusion

This paper introduced a novel Reliability-Based Multi-Lattice Topology Optimization framework that integrates surrogate modeling, numerical homogenization, and probabilistic design principles for optimizing multiscale lattice-structured components under uncertainty. Motivated by the hierarchical and adaptive nature of biological and architected materials, the proposed approach enables the spatial distribution of multiple anisotropic lattice unit cells across a macrostructure, accounting for stochastic variations in material properties and loading. To address the computational challenges associated with high-resolution lattice modeling, a Kriging-based surrogate model was developed to approximate the effective constitutive behavior of lattice structures as a function of relative density. This significantly reduced the cost of iterative finite element analyses during topology optimization while preserving accuracy. The framework also employed a single-loop approximation for reliability evaluation, allowing efficient handling of probabilistic constraints without nested optimization. Overall,

the RBMTO framework offers a computationally efficient methodology for optimizing lightweight, reliable, and multi-lattice structures under uncertainty.

REFERENCES

[1] Bendsøe, M. P., & Sigmund, O. (2004). *Topology Optimization: Theory, Methods, and Applications*. Springer.

[2] Carbonari, L., Lamberti, L., & De Litio, A. (2007). Topology optimization of piezoelectric linear actuators with electro-mechanical coupling. Computers & Structures, 85(11–14), 891–904.

[3] Krog, L., Tucker, A., & Rollema, G. (2004). Topology optimization of aircraft wing box ribs. In 10th AIAA/ISSMO Multidisciplinary Analysis and Optimization Conference.

[4] Sutradhar, A., Paulino, G. H., Miller, M. J., & Nguyen, T. H. (2010). Topology optimization for cranial implants. Computer Methods in Applied Mechanics and Engineering, 197(51–52), 5152–5166.

[5] Chun, J., Song, J., and Paulino, G. (2016). Structural topology optimization under constraints on instantaneous failure probability. Structural and Multidisci plinary Optimization, 53(4).

[6] Chun, J.,Song, J., and Paulino, G. H. (2019). System reliability-based design and topology optimization of structures under constraints on first-passage probability. Structural Safety, 76, 81–94.

[7] Banh, T. T., Luu, N. G., and Lee, D. (2021). A non-homogeneous multi-material topology optimization approach for functionally graded structures with cracks. Composite Structures, 273, 114230.

[8] Sanders, B., Aguiló, M. A., and Paulino, G. H. (2018). Multi-material continuum topology optimization with arbitrary volume and mass constraints. Computer Methods in Applied Mechanics and Engineering, 340, 798–823.

[9] Wu, J., & Wang, C. C. L. (2018). Integrated topology optimization and design of lattice infill structures for additive manufacturing.Computer-Aided Design, 80, 1–13.

[10] Xue, Y., Zhang, J., & Wang, Y. (2023). Data-driven topology optimization of lattice structures using graph convolutional networks. Structural and Multidisciplinary Optimization, 67, 785–801.

[11] Guedes J. & Kikuchi N.(1990). Preprocessing and postprocessing for materials based on the homogenization method with adaptive finite element methods, Computer Methods in Applied Mechanics and Engineering, vol. 83, no. 2, pp. 143–198.

[12] Der Kiureghian, A. (2005). First- and Second-Order Reliability Methods. Engineering Design Reliability Handbook, CRC Press, Boca RatoN, Chapter 14.

[13] B. Echard, N. Gayton, M. Lemaire. AK-MCS: An active learning reliability method combining Kriging and Monte Carlo Simulation, Structural Safety, Volume 33, Issue 2, 2011, Pages 145-154,